DISTRIBUTED PROPELLERS SLIPSTREAM EFFECTS ON WING AT LOW REYNOLDS NUMBER

Wang Kelei[1, 2], Zhu Xiaoping[2], Zhou Zhou[1, 2]
1. College of Aeronautics, Northwestern Polytechnical University
2. Science and Technology on UAV Laboratory, Northwestern Polytechnical University

Keywords: *HALE solar-powered UAVs; low Reynolds numbers; distributed propellers/wing integration; slipstream aerodynamic effects*

Abstract

Based on the research about the distributed electric propulsion (DEP) technology applied on high-altitude long-endurance (HALE) solar-powered unmanned aerial vehicles (UAVs), the aerodynamic characteristics of the FX 63-137 wing under the distributed propellers slipstream effects in a tractor configuration at low Reynolds numbers are numerically studied. The numerical simulations are achieved by quasi-steadily solving the Reynolds-Averaged Navior-Stokes (RANS) equations based on the multiple reference frames (MRF) method, the k_T-k_L-ω transition model, and the hybrid grids. Firstly, the numerical results of the FX 63-137 wing and a practical propeller X1 are compared with the experimental data to validate the accuracy and flexibility of the method. Secondly, the aerodynamic properties of the distributed propellers/wing integration are compared among different rotation rates of propellers. Lastly, the detailed flow structures formed on the wing surfaces are sketched and analyzed. The results show that (a) significant lift benefits can be achieved for the reason that both the speed and the dynamic pressure of the incoming flow are enhanced by the propellers slipstream; (b) the turbulence added to the free stream by means of the distributed propellers slipstream prevent the formation of laminar separation bubble (LSB), but apparent horizontal vortexes can be observed at the slipstream boundaries at the same time; (c) the lift augmentation on the down-wash side of the wing is slightly stronger than that on the up-wash side at low Reynolds numbers, which results from the mechanisms that the LSB formed on the windward side of the wing is correspondingly found to be slightly shorter than that on the leeward side.

1 Introduction

Due to the depletion of fossil fuels and the occurrence of environmental problems, solar is seemed to be the most promising clean energy in the future, thus the development of high-altitude long-endurance (HALE) solar-powered unmanned aerial vehicles (UAVs) has nowadays attracted considerable interests. Since the successes of the first solar flight by the Sunrise I in 1974[1], great achievements have been maed by NASA series of solar aircrafts[2]. However, the advanced application of the distributed electric propulsion (DEP) technology[3-5], such as the 14 distributed propellers mounted on the "Helios", has raised a number of important engineering issues of concern, among which the most important and difficult problem is the mutual interferences between distributed propellers and the wing.

It appears that the propeller/wing interaction has been the subject of study for decades[6-9], however, most of the theoretical and experimental work were concentrated on the effects induced by an isolated propeller. It is necessary to have more accurate modeling to analyze the multiple propellers slipstream effects. Recently, Patterson and German[10,11] modeled the aerodynamics of the Leading Edge Asynchronous Propulsion Technology (LEAPTech) wing by employing the distributed vorticity element (DVE) method, which only takes one-way influences of the propellers on the wing into consideration. Alex[12] analyzed the LEAPTech wing aerodynamic performances among several kinds of numerical results and the experimental data, and then pointed out that the numerical results could show the wing aerodynamic trends similarly with that the experiment did, and that the relative errors (less than 10%) achieved were deeply related to the degree of simplifications.

The researches on the distributed propellers slipstream effects discussed heretofore are primarily based on the assumption of the simplified non-rotational and non-viscous flow. However, currently HALE solar-powered UAVs also tend to operate in the low density and low speed flight conditions, in which the interesting but complex viscous flow structures[13-15] will be formed at low Reynolds numbers. Hence, the combined aerodynamic effects of the low Reynolds conditions and the distributed propellers slipstream should be paid great attention to when studying the distributed propellers/wing integration.

With the aim of providing deep insights into the complex aerodynamic processes of the distributed propellers/wing interferences at low Reynolds numbers, a detailed numerical study of the wing aerodynamic performances and boundary layer behaviors under the distributed propellers slipstream effects at a Reynolds number of 3.0×10^5 is conducted in the present paper by employing the computational fluid dynamic (CFD) methods.

2 CFD Methods

Based on the multiple reference frames (MRF) method[16] and the structured-unstructured hybrid grids, the quasi-steady numerical simulations are obtained by solving the Reynolds-Averaged Navior-Stokes (RANS) equations coupled with the k_T-k_L-ω transition model[17], applying a standard cell-centered finite-volume scheme for the discretization, and using the LU-SGS implicit solution and the Roe format for the spatial discretization.

2.1 MRF Method

Compared with the unsteady simulation methods, the quasi-steady method based on the MRF systems is able to show satisfied accuracy while the computational resources can be greatly saved at the same time.

The application of the MRF method can be described as three steps: (a) dividing the computational region into two parts: the static region for the wing and the rotational region for each propeller; (b) building different moving reference frame for each rotational region; (c) simulating the whole flow field through grids mutual information communications on the interfaces among different regions.

The governing equations in integral form for the rotating coordinate systems can be written as follows[16]:

$$\frac{\partial}{\partial t}\iiint_{V}\mathbf{Q}\,dV+\oiint_{\partial V}\mathbf{H}\cdot\mathbf{n}\,dS-\oiint_{\partial V}\mathbf{H}_{V}\cdot\mathbf{n}\,dS+\iiint_{V}\mathbf{G}\,dV=0 \quad (1)$$

where

$$\mathbf{Q}=[\rho,\rho u,\rho v,\rho w,\rho E]^{\mathrm{T}} \quad (2)$$

$$\begin{aligned}\mathbf{H}=[&\rho(\mathbf{q}-\mathbf{q}_b),\rho(\mathbf{q}-\mathbf{q}_b)+p\mathbf{I}_x,\rho(\mathbf{q}-\mathbf{q}_b)+p\mathbf{I}_y,\\&\rho(\mathbf{q}-\mathbf{q}_b)+p\mathbf{I}_z,\rho H(\mathbf{q}-\mathbf{q}_b)+p\mathbf{q}_b]^{\mathrm{T}}\end{aligned} \quad (3)$$

$$\begin{aligned}\mathbf{H}_{V}=[&0,\tau_{xx}\mathbf{I}_x+\tau_{xy}\mathbf{I}_y+\tau_{xz}\mathbf{I}_z,\tau_{xy}\mathbf{I}_x+\tau_{yy}\mathbf{I}_y+\tau_{yz}\mathbf{I}_z,\\&\tau_{zx}\mathbf{I}_x+\tau_{zy}\mathbf{I}_y+\tau_{zz}\mathbf{I}_z,f_5\mathbf{I}_x+g_5\mathbf{I}_y+h_5\mathbf{I}_z]^{\mathrm{T}}\end{aligned} \quad (4)$$

$$\mathbf{G}=\left[0,\rho(\boldsymbol{\omega}\times\mathbf{q})_x,\rho(\boldsymbol{\omega}\times\mathbf{q})_y,\rho(\boldsymbol{\omega}\times\mathbf{q})_z,0\right]^{\mathrm{T}} \quad (5)$$

V is the fluid control body, and ∂V is the boundary surface of the control body. ρ is the air density. u, v, w are the three components of velocity vector in the Cartesian coordinate system, E is the internal energy, $\mathbf{I}_x$, $\mathbf{I}_y$, $\mathbf{I}_z$ are respectively the unit vectors in three directions of Cartesian coordinate system, $\mathbf{q}$ is the absolute velocity vector, $\mathbf{q}_b$ is the grid velocity vector, τ is the shear stress, $\boldsymbol{\omega}$ is the angular velocity vector of the rotating parts. f_5, g_5, h_5 can be expressed as follows:

$$f_5=u\tau_{xx}+v\tau_{xy}+w\tau_{xz}+k\frac{\partial T}{\partial x} \quad (6)$$

$$g_5=u\tau_{xy}+v\tau_{yy}+w\tau_{yz}+k\frac{\partial T}{\partial y} \quad (7)$$

$$h_5 = u\tau_{xz} + v\tau_{yz} + w\tau_{zz} + k\frac{\partial T}{\partial z} \tag{8}$$

T is the temperature, k is the heat transfer coefficient.

2.2 Hybrid Grids

Corresponding to the two computational regions of the MRF method, the structured-unstructured hybrid grids are generated. As shown in Fig.1, to obtain less and higher-quality mesh, the structured grids with a number of nearly 4.5 million are applied in the static region of the wing, and to reduce the difficulty of complex geometry (propeller) mesh generating processes, the unstructured grids with a number of nearly 2.0 million are applied in the rotational region of each propeller. In addition, the far-field boundaries of the static region are located at a distance of 35 chords from the wing, and the rotational region of each propeller is defined as a cylindrical form around the propeller with a thickness of 0.1m and a diameter of 0.27m.

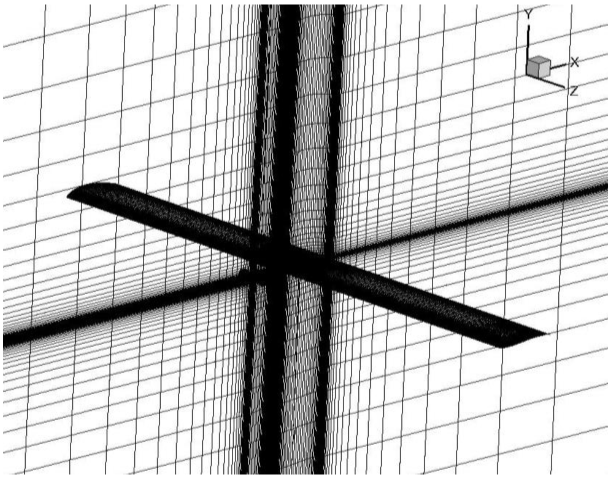

(a) Sectional View of Structured Grids

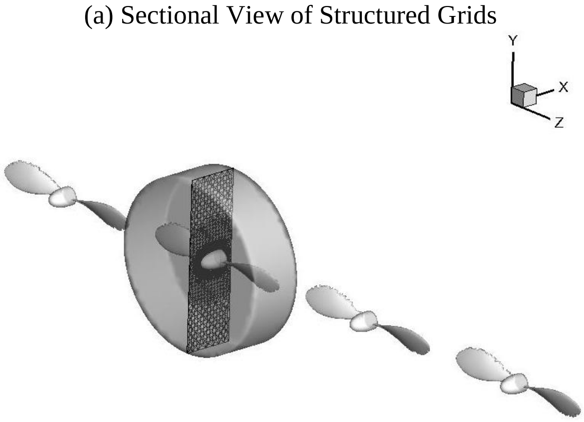

(b) Sectional View of Unstructured Grids

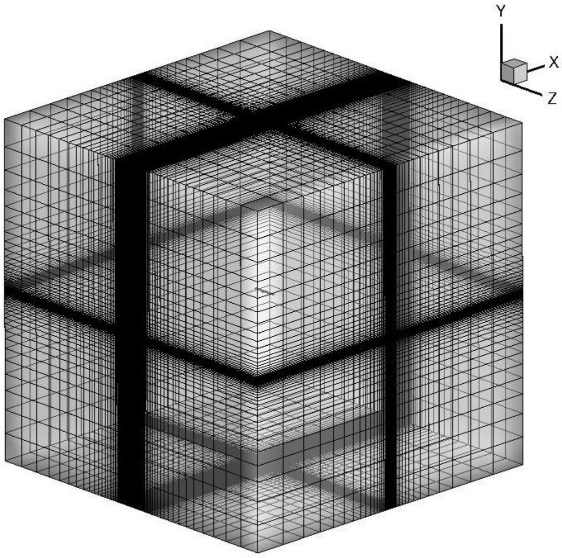

(c) View of Grids on the Far-Field Surfaces

Fig. 1. Structured-Unstructured Hybrid Grids

2.3 Transition Model

The k_T-k_L-ω transition model is based on the simulation of stream-wise fluctuation in terms of the laminar kinetic energy. The growth of the laminar kinetic energy is explained by the splat mechanism proposed by P. Bradshaw[18], and discussed in more details by R. J. Volino[19]. In our research, the stream-wise fluctuations are considered to exist in the pre-transitional region of the boundary layer and in the application of an eddy viscosity approach.

With the theory described above, a turbulence transition model including three transport equations for laminar kinetic energy (k_L), turbulent kinetic energy (k_T) and inverse turbulent time scale (ω) is introduced by Walters and Cokljat[17]. In this model, predicting the onset of transition is based on a local parameter of the turbulent energy and effective length scale, it is considered that the transition begins and the energy from the stream-wise fluctuations (k_L) converts into the turbulent fluctuations (k_T) in the boundary layer when this parameter increases to a prescribed value. Besides, ω is used as the scale-determining variable that can lead to a reduced intermittency effect in the outer region of the boundary layer, As a result, an elimination of the wake region in the velocity profile can be achieved[20].

The transport equations of k_T-k_L-ω transition model in an incompressible form can be written as follows:

$$\frac{dk_T}{dt} = P_{k_T} + R + R_{NAT} + \frac{\partial}{\partial x_j}\left[\left(v + \frac{\alpha_T}{\alpha_k}\right)\frac{\partial k_T}{\partial x_j}\right] - \omega k_T - D_T \tag{9}$$

$$\frac{dk_L}{dt} = P_{k_L} - R - R_{NAT} - D_L + \frac{\partial}{\partial x_j}\left(v\frac{\partial k_L}{\partial x_j}\right) \tag{10}$$

$$\frac{d\omega}{dt} = C_{\omega 1}\frac{\omega}{k_T}P_{k_T} + \left(\frac{C_{\omega R}}{f_W} - 1\right)\frac{\omega}{k_T}(R + R_{NAT}) + C_{\omega 3} f_\omega \alpha_T f_W^2 \frac{\sqrt{k_T}}{d^3} + \frac{\partial}{\partial x_j}\left[\left(v + \frac{\alpha_T}{\alpha_\omega}\right)\frac{\partial \omega}{\partial x_j}\right] - C_{\omega 2}\omega^2 \tag{11}$$

Refer to ref.17 for definitions and values of the parameters if necessary.

3 Validation

To assess the accuracy and flexibility of the CFD method described above, we carry out two studies on the basis of experimental data, the first is the FX 63-137 wing case study[21], and the second is the propeller case study[22].

3.1 Wing Case

According to [21], an isolated Wortmann FX 63-137 wing with a chord of 1.6 m and AR of 8.9 is numerically simulated. The simulatin setting is: H=20km, V=30m/s, Re_c=3.0×10^5, Tu_∞=0.1%. To eliminate the influences of grid type differences, both the structured grids and the structured-unstructured hybrid grids are numerically studied compared with the experimental data.

As shown in Fig. 2, at nearly all the angles of attack (AOA) studied, the numerical results are very similar to the experimental data for both the structured and the hybrid grid types, and only less-than-3% differences can be found between the numerical results and the experimental data. But with the AOA reaching up to 14°, the experimental lift coefficient appears to have a more notable nonlinear increment than that of the numerical results. Besides, approximately less-than-0.8% numerical differences can be found between these two types of grids, which indicates that the way to generate unstructured grids in some regions has little influence on the calculation precision.

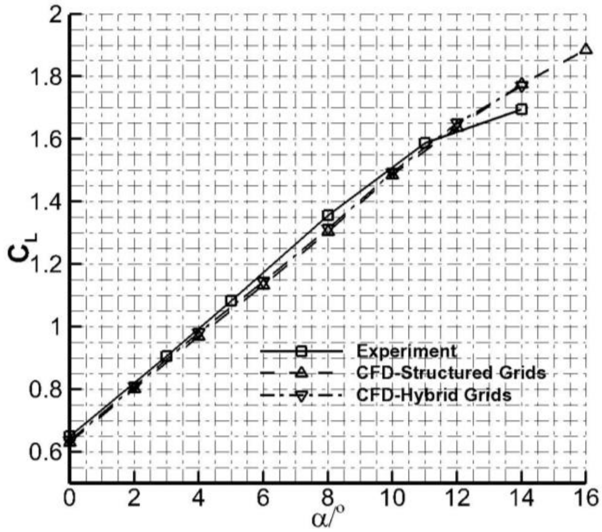

(a) C_L-α

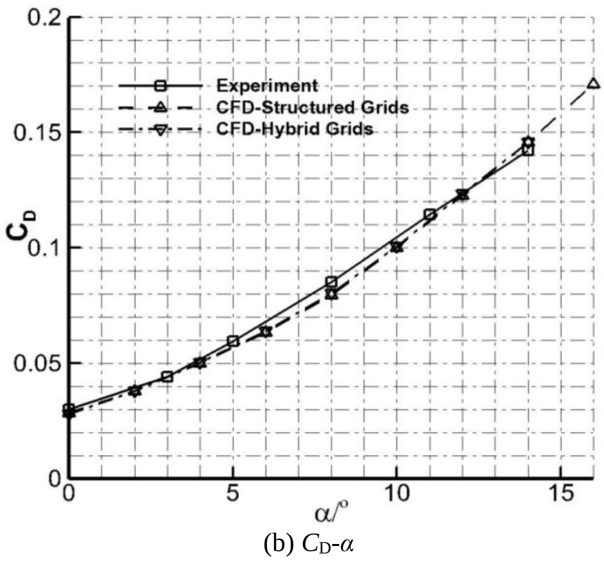

(b) C_D-α

Fig. 2. Comparison of Wing Aerodynamic Properties between the Numerical and Experimental Results

Fig. 3 shows the detailed flow structures including the near-wall streamline shapes and the turbulent kinetic energy distributions on the surfaces of the FX 63-137 wing at α=0°.

It indicates that at the low Reynolds number of 3.0×10^5, except for the strong influences of the roll-up vortexes around the wingtip, obvious phenomenon of "laminar separation", "transition", and "turbulent reattachment" can be observed to be distributed smoothly in the span-wise direction on both the upper and the lower surfaces of the FX 63-137 wing. Besides, a shorter laminar separation bubble (LSB) on the lower surface can be found to be formed earlier than the LSB formed on the upper surface. Obviously, the present CFD method has the ability to adequately simulate the complex aerodynamic processes at low Reynolds numbers.

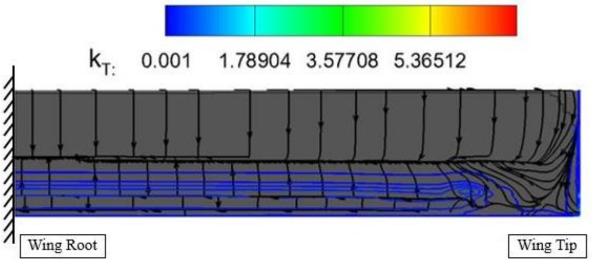

(a) Upper Surface

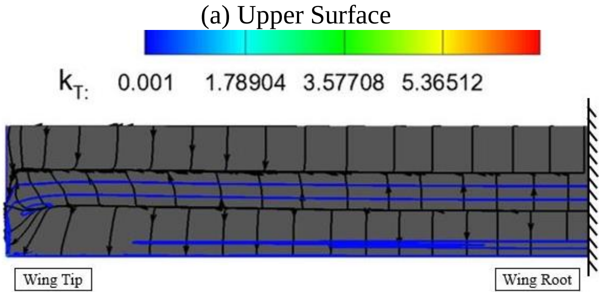

(b) Lower Surface

Fig. 3. Detailed Flow Structures on the Surfaces of the FX 63-137 Wing at α=0°

3.2 Propeller Case

According to [22], a practical propeller named "X1" with a diameter of 1.2 m is numerically studied. The simulation parameters are chosen as follows: V=13m/s, n=1200rpm, 1500rpm, 1800rpm, and 2000rpm, and then the 0.7R-section characteristic Reynolds numbers of 7.72×10^5, 9.55×10^5, 1.14×10^6, and 1.26×10^6 can be separately achieved corresponding to these rotation rates. Fig. 4 shows the comparisons of the propeller thrust properties between the numerical and experimental results.

It seems that the calculated propeller thrust is always less than the experimental data, and a less-than-10% relative error can be achieved at all the AOAs studied. Besides, with the rotation rate increasing, the numerical error is getting larger and larger, which may be due to the limitations of the transition model to simulate the flow with a continuously increasing characteristic Reynolds number.

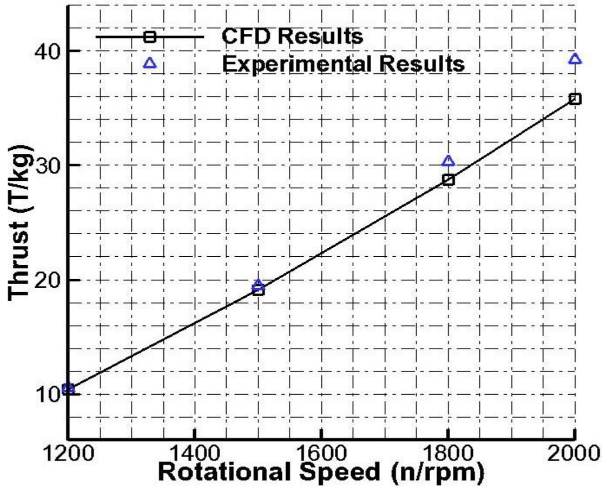

Fig. 4. Comparison of X1 Propeller Thrust Properties between the Numerical and Experimental Results

4 Results and Discussion

As shown in Fig. 5, the "Fpro" model, which includes a FX 63-137 wing as the same as that in the wing case and four distributed propellers of X1 with a diameter of 0.25 m, are numerically studied. In the present tractor configuration, propellers are located in the middle of the wing. The distance between every two adjacent propellers is 0.3 m, and the distance from each propeller to the wing is 0.8 m. All these propellers are rotating synchronously in the clockwise direction along the streamlines, and they are individually named as Pro1, Pro2, Pro3 and Pro4 from left to right to make a distinction.

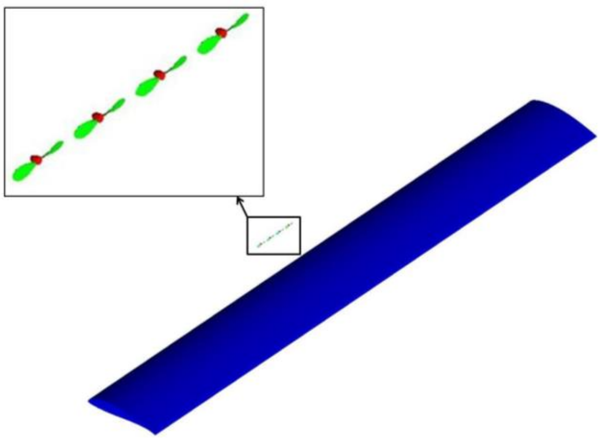

Fig. 5. Four Propellers/Wing Simplified Model

The simulation parameters are chosen as follows: H=20km, V=30m/s, Re_c=3.0×105, Tu_∞=0.1%, and to meet the power demands of different flight stages, varied rotation rates of the propellers in the range from 12000 rpm to 18000 rpm are numerically studied.

4.1 Thrust Property of Distributed Propellers

The relationship between the total thrust and rotation rate of the distributed propellers is shown in Fig. 6.

It can be found that in the present tractor configuration, the existence of the wing can enlarge the thrust of the propellers to some extent, and a maximum increment of relatively 4.4% can be obtained at n=18000 rpm.

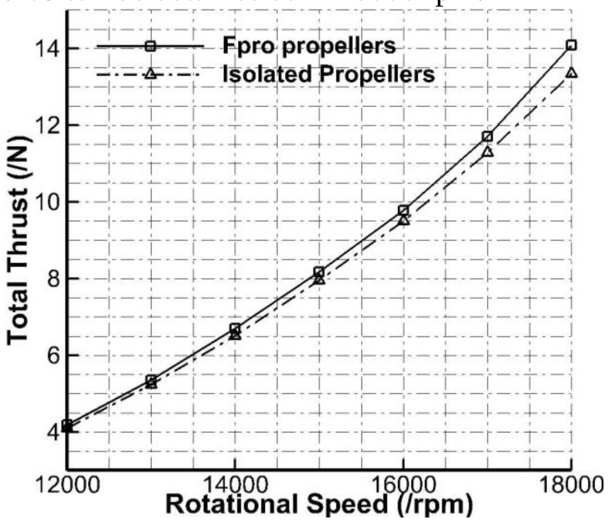

Fig. 6. Curve of the Total Thrust-to-Rotation rate of Propellers at α=0。

4.2 Aerodynamic Performances of Wing

Three test cases with rotation rates of 12000rpm, 15000rpm, and 18000rpm are numerically studied.

Fig. 7 shows the comparison of wing aerodynamic forces under the effects of distributed propellers slipstream with respect to the clean wing case.

It suggests that even with propellers not designed for lift augmentation, lift benefits can be observed at all AOAs studied, and the lift of wing significantly increases as the rotation rate of propellers increases. This is mainly due to the acceleration of the air speed and the enhancement of the dynamic pressure.

Besides, it is also important to note that the wing exhibits significantly increased drag characteristics due to the propellers slipstream effects, and there is an increase in drag as the rotation rate of propellers increases.

In addition, a slight reduction in lift curve slope and a slight increment in drag curve slope are observed for all the test cases with respect to the clean wing case, and as the propellers rotation rate increasing, negligible variation in both the wing lift curve slope and the wing drag curve slope is found.

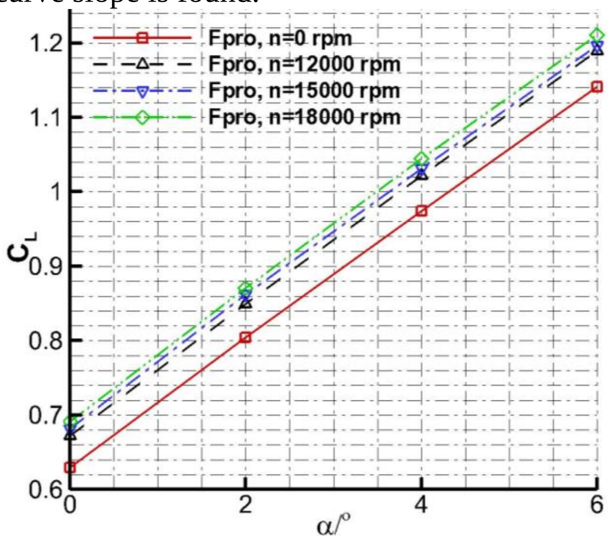

(a) C_L-α

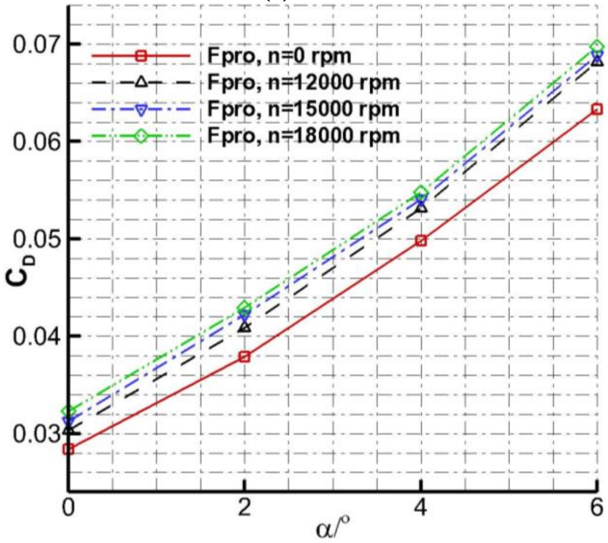

(b) C_D-α

Fig. 7. Comparison of Wing Aerodynamic Performance

Fig. 8 shows the comparison of wing lift distributions in span-wise direction between the wing case and three test cases, in which the wing is evenly divided into 40 parts and the lift coefficient of each part (c_l) is calculated with the total area of the wing as the reference area.

The "Up-wash" and "Down-wash" indicate the rotation directions of the distributed propellers.

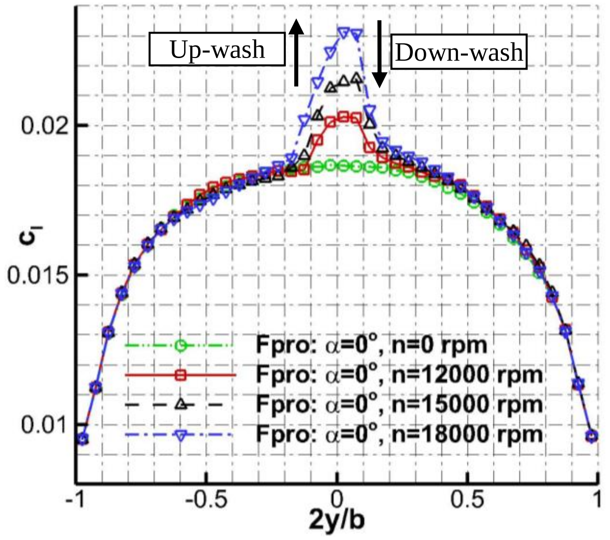

Fig. 8. Comparison of Wing Lift Distribution in Span-Wise Direction at α=0°

It shows that within the region $-0.2\leq 2y/b\leq 0.2$, apparent lift augmentation induced by the propellers slipstream can be observed on both the up-wash side (UWS) and the down-wash side (DWS), and the lift augmentation is continuously increasing as the propellers rotation rate increases.

Besides, the lift distribution curves of the three test cases show significantly different features from that the typical conventional propeller/wing integration shows: the lift generated on the UWS is slightly less than that on the DWS. This may be related to the differences of boundary layer behaviors on the wing surfaces between UWS and DWS.

4.3 Detailed Boundary Layer Behaviors

In order to investigate the general feature and law of the aerodynamic properties of the distributed propellers/wing integration at low Reynolds numbers, the detailed boundary layer behaviors of the Fpro model at n=15000rpm is further analyzed.

Fig. 9 shows the distributions of both the near-wall streamline and the turbulent kinetic energy on the upper surface of the FX 63-137 wing.

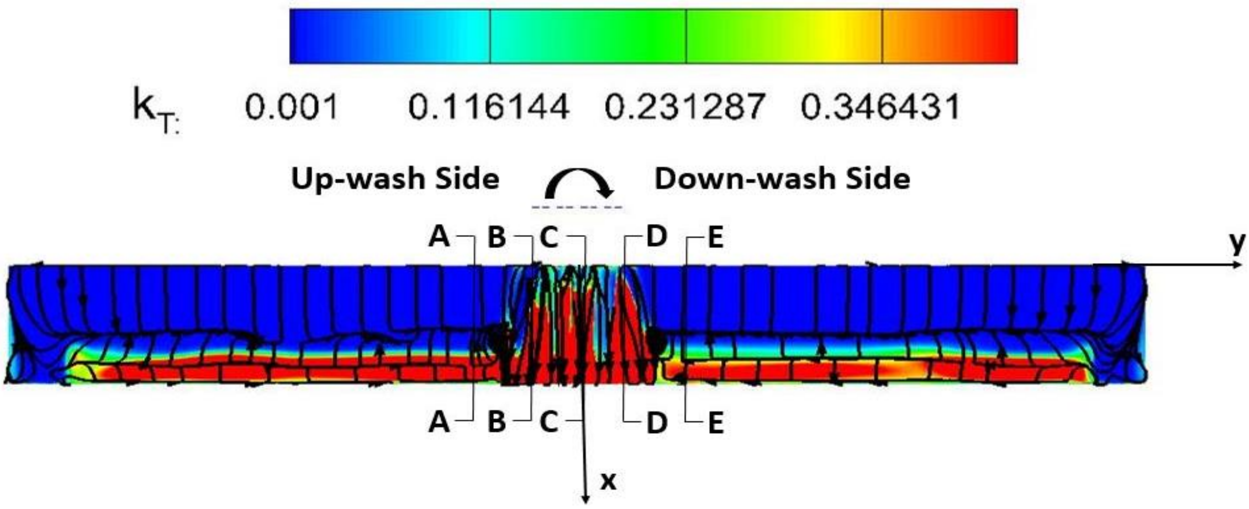

(a) Upper Surface

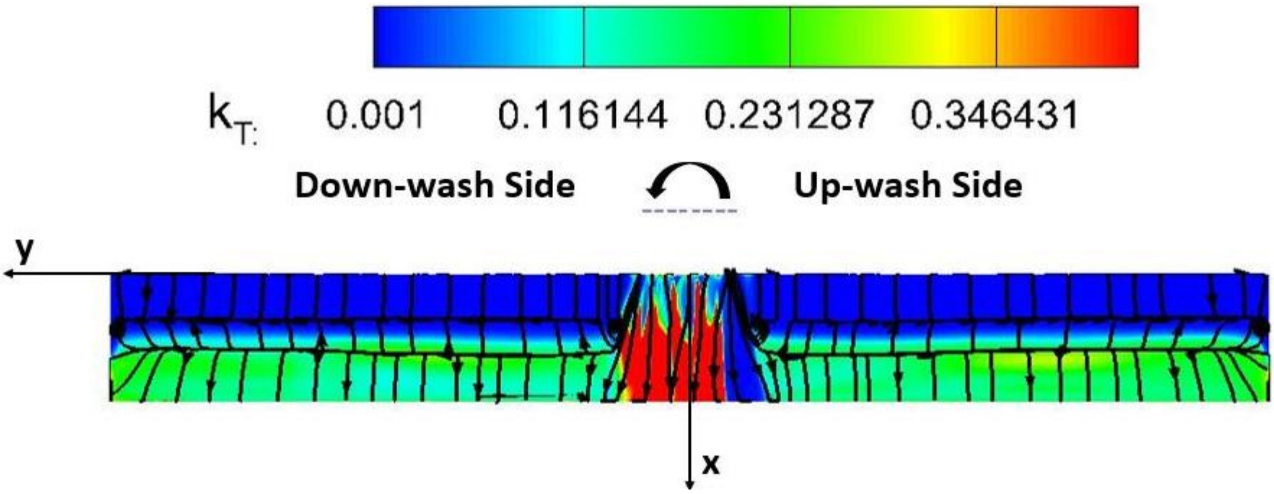

(b) Lower Surface

Fig. 9. Detailed Flow-Field Characters on the Wing surfaces at α=0° and n=15000rpm

It obviously shows that (a) the turbulence added to the free stream by means of the distributed propellers slipstream enhances the flow's ability to resist strong adverse pressure gradient, which causes the typical LSB to vanish on both surfaces of the wing; (b) the span of the turbulent-attached region affected by the distributed propellers slipstream is found to be about 1.4 times of the sum of propellers diameters; (c) significant horizontal vortexes are observed to be formed along the boundaries of the turbulent-attached region, and the centers of the vortexes are located at nearly 0.6 times (vortexes on the upper surface) and 0.34 times (vortexes on the lower surface) of the wing chord in the stream-wise direction; (d) with respect to the UWS (leeward side) on the upper surface, the phenomenon of "turbulence reattachment" occurs at an earlier position, and the turbulence abundance reduces to a lower level on the DWS (windward side), which may be the reason why the lift augmentation on the DWS is non-empirically larger than that on the UWS.

To conceptualize the features described above, the comparison of pressure distributions among airfoils at section A (y=-1.0), B (y=-0.55), C (y=0.0), D (y=0.55), and E (y=1.0) is given in Fig. 10.

It shows that the existence of the propellers leads to an increment of the suction peak at the leading edge (LE) of the wing, and also leads to the disappearance of the pressure platform in the recovery range of the wing, which directly introduces lift benefits. Besides, the suction peak at section B is stronger than that at section D, which is consistent with the up-wash effects and down-wash effects caused by the rotational propellers. In addition, the pressure distribution at section C is between that at section B and D, which may be due to the fact that the down-wash effects from the right two propellers and the up-wash effects from the left two propellers are so opposed that they just cancel each other, and as a result, the wing behind the propellers are mainly experiencing the propeller-induced acceleration effects.

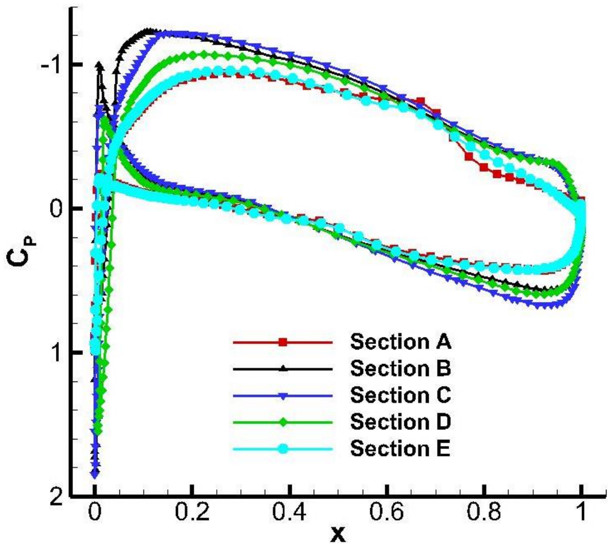

Fig. 10. Comparison of Pressure Distributions among Different Sections at α=0° and n=15000rpm

5 Conclusions

To investigate the aerodynamic effects of the distributed propellers slipstream on the FX

63-137 wing at the low Reynolds number of 3.0×10^5. Comparison of wing lift-drag forces among varied propeller rotation rates is conducted, and detailed boundary layer behaviors on the wing surfaces are analyzed. Results obtained in this study can be summarized as follows:

1. Apparent augmentations of both the lift and the drag forces can be obtained at the low Reynolds number of 3.0×10^5 due to the propeller slipstream effects.
2. The turbulence added to the free stream by means of the distributed propellers slipstream prevents the formation of LSB, but at the same time, apparent horizontal vortexes can be observed along the slipstream boundaries.
3. The turbulence abundance and the LSB formed on the upper surface of the wing on the windward side are lower and shorter than those on the leeward side, which results in a higher lift distributions on the windward side.
4. In the regions between two adjacent propellers, the down-wash effects from one propeller and the up-wash effects from another are so opposed that they just cancel each other to some degree, and the dominated effect of the propeller slipstream here is the acceleration of inlet-flow speed.

References

[1] R J Bouncher. History of solar flight. AIAA/SAE/ASME 20th Joint Propulsion Conference, Cincinnati, OH, AIAA-84-1429, 1984.

[2] Noll T E, Ishmael S D, Henwood B, and et.al. Technical findings, lessons learned, and recommendations resulting from the Helios prototype vehicle mishap. NATO/RTO AVT-145 Workshop on Design Concepts, Processes and Criteria for UAV Structural Integrity, Neuilly-sur-Seine, France, paper 3.4, pp 1-18, 2007.

[3] Borer N K, Moore M D and Turnbull A. Tradespace exploration of distributed propulsors for advanced on-demand mobility concepts. 14th AIAA Aviation Technology, Integration, and Operations Conference, Atlanta, GA, AIAA 2014-2850, 2014.

[4] Patterson M D, Daskilewicz M J and German B J. Conceptual design of electric aircraft with distributed propellers: multidisciplinary analysis needs and aerodynamic modeling development. 52nd Aerospace Sciences Meeting, National Harbor, MD, AIAA 2014-0534, 2014.

[5] Mark D M, Bill F. Misconceptions of electric aircraft and their emerging aviation markets. 52nd Aerospace Sciences Meeting, National Harbor, MD, AIAA 2014-0535, 2014.

[6] Catalano F M. On the effects of an installed propeller slipstream on wing aerodynamic characteristics. Acta Polytechnica, Vol. 44, No. 3, pp 8-14, 2004.

[7] Makino Fumiyasu, Nagai Hiroki. Propeller slipstream interference with wing aerodynamic characteristics of Mars airplane at low Reynolds number. 52nd Aerospace Sciences Meeting, National Harbor, MD, AIAA 2014-0744, 2014.

[8] L Ting, CH Liu and G Kleinstein. Interference of wing and multi-propellers. AIAA 4th Fluid and Plasma Dynamics Conference, Palo Alto, CA, AIAA paper 71-614, 1971.

[9] Qin E, Guowei Yang and Fengwei Li. Numerical analysis of the interference effect of propeller slipstream on aircraft flowfield. Journal of Aircraft, Vol. 35, No. 1, pp 84-90, 1998.

[10] Patterson D M, German J B. Wing aerodynamic analysis incorporating one-way interaction with distributed propellers. 14th AIAA Aviation Technology, Integration, and Operations Conference, Atlanta, GA, AIAA 2014-2852, 2014.

[11] Patterson D M, German J B. Simplified aerodynamics models to predict the effects of upstream propellers on wing lift. 53rd AIAA Aerospace Sciences Meeting, Kissimmee, FL, AIAA 2015-1673, 2015.

[12] Alex M S. Comparison of CFD and experimental results of the LEAPTech distributed electric propulsion blown wing. 15th AIAA Aviation Technology, Integration, and Operations Conference, Dallas, TX, AIAA 2015-3188, 2015.

[13] Mark Drela. Low Reynolds number airfoil design for the M.I.T. Daedalus prototype: a case study. Journal of Aircraft, Vol. 25, No. 8, pp 724-732, 1988.

[14] Peng B, Erjie C and Weijiang Z. Numerical simulation of laminar separation bubble over 2D airfoil ay low Reynolds number. Acta Aerodunamica Sinica, Vol. 24, No. 4, pp 416-424, 2006.

[15] Kelei W, Zhou Z, Wenbiao G, and et.al. Studying aerodynamic performances of the low Reynolds number airfoil of solar energy UAV. Journal of Northwestern Polytechnical University, Vol. 32, No. 2, pp 163-168, 2014.

[16] Xiaoliang C, Jie L. Unsteady computational method for propeller/wing interaction. Science Technology and Engineering, Vol. 11, No. 14, pp 3229-3235, 2011.

[17] Walters D K, Cokljat D A. A three-equation eddy-viscosity model for Reynolds-averaged Navier-

Stokes simulations of transitional flows. Journal of Fluids Engineering, Vol. 130, No. 1, pp 1-14, 2008.
[18] Bradshaw P. Turbulence: the chief outstanding difficulty of our subject. Experiments in Fluids, Vol. 16, No. 3-4, pp 203-216, 1994.
[19] Volino R J. A new model for free-stream turbulence effects on boundary layers. ASME Journal of Turbomachinery, Vol. 120, No. 3, pp 613-620, 1998.
[20] *ANSYS FLUENT 12.0 Theory Guide-Turbulence*. 2009.
[21] Gregory A W, Bryan D M, Benjamin A B, and et.al. Summary of low-speed airfoil data Vol.5. Illinois: University of Illinois at Urbana-Champaign, 2012.
[22] Weijia F, Jie L and Haojie W. Numerical simulation of propeller slipstream effect on a propeller-driven unmanned aerial vehicle. Procedia Engineering, Vol. 31, pp 150-155, 2012.

6 Copyright Issues

7 Contact Author Email Address

ak203201@163.com